$$\frac{d\hat{\rho}_S}{dt} = \left(\hat{\hat{L}}_S - \left(k_{aE}[B_{H_2}] + k_{aA}[B_A] \right) \hat{\hat{1}}_S \right) \hat{\rho}_S + [B_{H_2}] \left(k_{aE}\,\hat{\mathrm{Tr}}_{H_2}(\hat{\rho}_{B_E}) + k_{aA}\,\hat{\mathrm{Tr}}_{H_2}(\hat{\rho}_{B_A}) \right)$$

$$\frac{d\hat{\rho}_{B_E}}{dt} = \left(\hat{\hat{L}}_{B_E} - k_{dE}\,\hat{\hat{1}}_{B_E} \right) \hat{\rho}_{B_E} + k_{dE}\,\hat{\rho}_{B_{H_2}} \otimes \hat{\rho}_S$$

Showcasing research from the Stevanato Lab at the University of Padova (IT)

(De)coding SABRE of [1-13C]pyruvate

The paper presents a combined synthetic, experimental, and theoretical study of seven Ir-NHC catalysts for SABRE hyperpolarization. IPr and SIPr emerge as effective alternatives to the benchmark IMes. A fast kinetic model incorporating experimental variables guides a temperature-jump experimental protocol that boosts the free pyruvate signal by ~30%, providing a rational framework to optimize SABRE for biomedical applications.

Image reproduced by permission of Federico Floreani, Salvatore Mamone and Gabriele Stevanato from *Phys. Chem. Chem. Phys.*, 2025, **27**, 22924.

Molecular structures created with Avogadro: http://avogadro.cc.

ROYAL SOCIETY OF CHEMISTRY

rsc.li/pccp

PCCP Owner Societies

Check for updates

(De)coding SABRE of [1-^{13}C]pyruvate

Salvatore Mamone, [ID] †[a] Federico Floreani, [ID] †[b] Ahmed Mohammed Faramawy, [ID] [b] Claudia Graiff, [ID] [c] Lorenzo Franco, [ID] [b] Marco Ruzzi,[b] Cristina Tubaro [ID] [b] and Gabriele Stevanato [ID] ★[b]

Hyperpolarized pyruvate is a key molecular probe for biomedical imaging but achieving efficient ^{13}C signal amplification by reversible exchange (SABRE) enhancement remains elusive. Here, we report a comprehensive study integrating catalyst design, systematic experimentation, and advanced theoretical modelling. We synthesized and tested seven Ir–NHC catalysts, spanning the main families of carbene ligands, including previously unexplored variants for pyruvate SABRE. IMes remains the benchmark, delivering ~3% ^{13}C polarization at 50% parahydrogen enrichment (extrapolated to ~10% at 100% parahydrogen), but structurally distinct alternatives such as IPr and SIPr achieve only ~20% lower performance, allowing detection of natural abundance ^{13}C signals in one scan at 1.4 T. DFT calculations indicate that J-couplings between hydrides and ^{13}C nuclei are similar across binding geometries and catalysts, indicating that exchange dynamics—rather than coupling strength—govern polarization efficiency. To clarify this, we performed variable-temperature experiments on both free and catalyst-bound pyruvate. To interpret the observed trends, we developed a detailed mechanistic model that incorporates species concentrations, parahydrogen fraction, exchange kinetics, spin couplings, and relaxation. By leveraging molecular symmetry to reduce Liouville space dimensionality, the model serves as an efficient and predictive tool for SABRE systems. Finally, we apply this framework to devise a SABRE protocol based on a temperature jump designed to selectively enhance the free pyruvate signal. This approach yields an ~30% increase in free pyruvate polarization at the expense of Ir catalyst-bound forms, with potential for further optimization. Altogether, our work bridges molecular design, theoretical modelling, and protocol development, offering a blueprint for the rational optimization of SABRE hyperpolarization of pyruvate and beyond.

Introduction

Nuclear magnetic resonance (NMR) and magnetic resonance imaging (MRI) are powerful techniques widely used across the chemical and life sciences. These include structural elucidation, reaction monitoring, disease screening, diagnosis, and assessment of treatment response.[1–3] This potential stems from their ability to probe site-specific chemical environments, the use of non-ionizing radiation, and relatively straightforward sample preparation. However, the intrinsically low sensitivity remains a fundamental roadblock for all conventional magnetic resonance techniques, in both NMR and MRI applications, posing a significant barrier to their broader use. Nuclear polarization quantifies the fraction of nuclear spins that

effectively contribute to the detectable NMR signal. At the largest commercially available magnetic field of ~28 T, the most used NMR probe, ^{1}H nuclei, has a polarization of about 5×10^{-5} at 298 K, meaning that ~5 nuclear spins in every 100 000 are responsible for the NMR signal. Low-gamma nuclei such as ^{13}C offer the advantage of resolving resonances over a wider frequency range than ^{1}H. However, they are significantly less sensitive, as the gyromagnetic ratio of ^{13}C is approximately one-fourth that of ^{1}H. Using lower magnetic fields further aggravates the NMR sensitivity limitations for all nuclei.

With only ~1 spin in 10^{6} contributing to the signal at 1 T, and a natural abundance of just ~1%, ^{13}C detection in a single scan at millimolar concentrations is challenging under standard conditions.

Hyperpolarization methods include all the strategies used to circumvent this problem united by the common goal of amplifying the magnetic resonance signal either in solution or in solid samples.[4] Dissolution dynamic nuclear polarization (dDNP) and spin-exchange optical pumping (SEOP) have been widely recognized as leading strategies for at least the last 20 years with ^{13}C polarization levels often larger than 50%.[5–9]

[a] *Dept. MESVA (Life, Health & Environmental Sciences), Università dell'Aquila, Via Vetoio SNC, Localita' Coppito, 67100 L'Aquila, Italy*

[b] *Dipartimento di Scienze Chimiche, Università di Padova, Via Marzolo 1, 35131 Padova, Italy. E-mail: gabriele.stevanato@unipd.it*

[c] *Dipartimento di Scienze Chimiche, della Vita e della Sostenibilità Ambientale, Università di Parma, Parco Area delle Scienze 17/a, 43124 Parma, Italy*

† These authors contributed equally.

22924 | *Phys. Chem. Chem. Phys.*, 2025, **27**, 22924–22936

This journal is © the Owner Societies 2025

Other methods using the nuclear singlet state of hydrogen (H_2) have emerged,[10–14] like parahydrogen induced polarization (PHIP) and PHIP-side arm hydrogenation (SAH) pairing the performance of dDNP for a large number of substrates.[8,15] Among the various polarized molecular systems, pyruvate emerges for its role in deregulated glycolytic pathways in diseases associated with inflammation, neurodegeneration, and cancer.[8,16–18] It was recently shown that [1,^{13}C]pyruvate can be hyperpolarized at about 10% and that [1,2-^{13}C]pyruvate, despite the overall lower signal amplification, might offer a viable option in specific cases thanks to NMR resonances occurring in different spectral regions.[19] Signal amplification by reversible exchange (SABRE) introduced by Duckett, Green and co-workers in 2009,[20,21] and further developed by many others,[8,16,22–31] also uses parahydrogen as a source of signal enhancement to hyperpolarize drugs, amino-acids and relevant metabolites including pyruvate.[20,32–37] The main advantage offered by SABRE as compared to PHIP-SAH is the possibility to perform multiple experiments on the same sample at a fraction of the cost of other technologies such as dDNP.[4,7,9,17,38–40] SABRE uses an Ir-based catalyst which transiently binds to parahydrogen and to the substrate of interest modulated by the presence of a sulfoxide co-ligand.[41] During the stochastic binding events the strong parahydrogen signal can be transferred to the substrate either by pulsed methods at high,[42,43] low magnetic fields[44–46] or by tuning the external main magnetic field to a suitable value as in the SABRE SHield enables alignment transfer to heteronuclei (SABRE-SHEATH) variant used here.[22,32,47]

Due to the reversible nature of the SABRE process, the experimental outcome relies not only on the mechanistic understanding of the coherent nuclear spin interactions occurring during the complex formation, but also on the nature of the catalyst and solvent used, on the level of parahydrogen enrichment, on the sample temperature, on the amount of dissolved H_2 and on the optimal ratio between the catalyst, substrate and co-ligand used to name a few parameters. A systematic and comprehensive approach can be highly beneficial in understanding this complex, multiparametric problem, enabling better control and prediction of experiments while also guiding the design of alternative synthetic routes for potential catalysts.

Here we present a detailed combined synthetic, experimental and theoretical investigation of seven Ir-based catalysts for SABRE hyperpolarization of [1-^{13}C]pyruvate, focusing on the temperature-dependent properties. We identify IPr and SIPr as catalysts for pyruvate that, in our experiments, show a performance comparable to the golden standard IMes within 20% (Fig. 1b).

To unravel the interplay of factors governing ^{13}C hyperpolarization, we developed a theoretical model building upon the previous work introduced by Ivanov et al. and further developed by Pravdivtsev et al.,[48–50] incorporating explicit dipolar relaxation, H_2 and substrate concentrations, the level of parahydrogen enrichment and reversible exchange kinetics for dihydrogen and substrate interactions with the Ir complex. Our model explicitly accounts for the important intermediate complex reported by
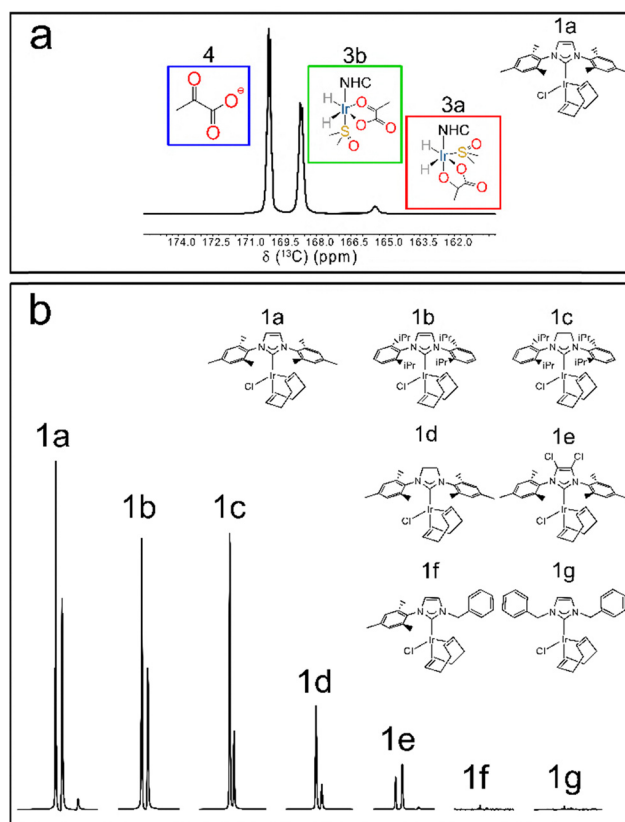

Fig. 1 (a) Single-scan hyperpolarized ^{13}C NMR spectrum of [1-^{13}C]pyruvate with the traces of free pyruvate (blue-framed box), equatorially bound **3b** pyruvate (green-framed box) and axially bound **3a** pyruvate (red-framed box). The sample consisted of 6 mM IMes (**1a**), 30 mM DMSO and 20 mM sodium [1-^{13}C]pyruvate in 700 μL of methanol-d$_4$. (b) The best acquired ^{13}C hyperpolarized NMR spectra and corresponding molecular structures of the catalysts investigated. All carbon spectra were recorded under conditions of saturated polarization at 280 K. The 700 μL NMR samples included in all cases 6 mM catalyst, 30 mM DMSO and 20 mM sodium [1-^{13}C]pyruvate in methanol-d$_4$. The spectra of **1f** and **1g** are amplified by a factor 10.

Tickner et al. mediating the parahydrogen (pH$_2$) exchange process.[41,51] By appropriately reducing the dimensionality of Liouville space matrices, we efficiently track the spin system's evolution, transforming this method into a powerful tool for advancing future SABRE investigations.

This study integrates three key aspects: detailed chemical synthesis, a simple experimental method, and a theoretical framework accompanied by effective numerical simulations. Building on these foundations, we also propose and apply a SABRE protocol based on a temperature jump, specifically designed to selectively enhance the free pyruvate signal. As a result, despite a parahydrogen enrichment of only 50%, we achieved hyperpolarization levels sufficient to perform ^{13}C NMR on pyruvate at natural abundance in a single scan with both IMes and IPr. This new protocol, which naturally arises from the proposed theoretical analysis, yields a ∼30% increase in free pyruvate polarization at the expense of the catalyst-bound forms, with potential for further optimization.

This journal is © the Owner Societies 2025

Phys. Chem. Chem. Phys., 2025, **27**, 22924–22936 | **22925**

Materials and methods

NMR experiments

Each NMR sample contained 6 mM activated catalyst (chemical synthesis and characterization in SI-1), 30 mM DMSO (unless stated otherwise), and 20 mM sodium [1-^{13}C]pyruvate in methanol-d$_4$, for a total volume of 700 μL in a 5 mm o.d. NMR tube. The hyperpolarization SABRE-SHEATH experiments were performed at 50% parahydrogen and 6 bar pressure, with a flux in the range of 80–150 sccm, at an optimal 0.33 μT magnetic field and a temperature of 240–310 K (magnetic field profiles in Section SI-6 and Fig. SI-17). The experimental set-up used is described in detail in Section SI-12, in figures Fig. SI-32–SI-34. Briefly, it consists of a mu-metal shield equipped with a solenoid coil connected to a power supply to produce the longitudinal desired magnetic field in the range 0–10 μT. 5 mm o.d. NMR sample tubes were inserted into a Wilmad suprasil VT dewar and their temperature was controlled by a cold nitrogen gas flow, temperature-regulated using a Bruker BVT2000 unit. The temperature was varied in the range of 240–310 K. The custom-made liquid-nitrogen-based parahydrogen delivery system (50% parahydrogen) is equipped with pressure regulators, in-line micro filters, safety valves, a mass flow controller, a backpressure regulator and ARDUINO-controlled electrovalves for parahydrogen bubbling.
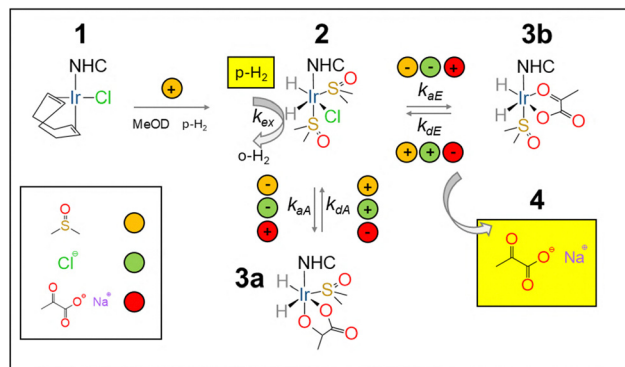
DFT calculations

The spatial configuration and the spin couplings of the bound species have been determined by DFT calculations using ORCA v6.0.1.[52–67] Geometries have been optimized using the TPSSh functional in combination with the def2-TZVP basis set (extended to def2-TZVPP for Ir) and the auxiliary basis set def2/J and using the options DEFGRID3 and TightSCF for numerical integration and convergence control. It is worth noticing that the def2 basis sets include ECP corrections for heavy elements in ORCA. The optimized geometries were confirmed to be local minima of the energy by running frequency calculations at the same level of theory of the geometry optimization. Spin couplings and chemical shifts have been calculated on the optimized geometries invoking the two-components approximation to treat relativistic effects (x2c keyword), using the TPSSh functional in combination with the decontracted x2c-QZVPPAll-2c basis set and the auxiliary basis set x2c/J maintaining the same options as in geometry calculations (DEFGRID3 and TightSCF). The tables of the optimized geometries and chemical shifts/spin couplings in the equatorial and axial configurations for each complex considered here are reported in the SI (see SI-DFT).

Simulations and numerical calculations

The complete SABRE spin dynamics is described by the system of differential equations contained in (1). All the numerical handling was done in Wolfram Mathematica,[68] including the matrix representation of operators and superoperators, the solution of the differential system (*via* the routine NDSolve), the calculation of expectations values and polarization levels and associated plots.

Results and discussion

The SABRE process for pyruvate has been rationalized as depicted in Scheme 1, as proposed by Duckett and coworkers in ref. 51. The NHC precatalyst **1** is activated in methanol-d$_4$ under about 30 sccm pH$_2$ flow at 6 bars pressure for about 30 minutes at 240 K. The sulfoxide complexes forming in the case of pyruvate SABRE experiments exhibit a different catalysis than that for other commonly observed N-donor substrates such as pyridine. While [Ir(H)$_2$(κ^2-pyruvate)(DMSO)(NHC)] (**3**) is the active polarization transfer catalyst for free ^{13}C pyruvate, the necessary hydrogen exchange is mediated by the complex ([IrCl(H)$_2$(DMSO)$_2$(NHC)]) (**2**).[41,51,53] Depending on the κ^2-pyruvate coordination geometry, the forms **3a** (the bound axial form later denoted in the model as B$_A$) and **3b** (the equatorial bound form later denoted as B$_E$) differentiate and are visible as distinct peaks at 1.4 T (see Fig. 1a). An alternative assignment for the bound axial form **3a** has also been reported.[41,67,69] Building on the gold-standard IMes (**1a**) catalyst, we explored six additional Ir-based SABRE catalysts, representing prototypes of symmetric (IPr (**1b**), SIPr (**1c**), SIMes (**1d**), IMesCl$_2$ (**1e**), and IBn (**1g**)) and asymmetric (IMesBn (**1f**)) designs (Fig. 1b). These Ir-based catalysts differ only for the coordinated NHC ligand, which influences steric hindrance around the metal center, exchange ligand dynamics, and electron density at the metal center. This last characteristic is primarily dependent on variation in either the imidazole 4,5-backbone (saturated version as for **1c** and **1d** or presence of chloro substituents as for **1e**) or in the nitrogen wingtip substituents (aryl or alkyl groups). Among them, the symmetric IPr (**1b**), SIPr (**1c**) and asymmetric IMesBn (**1f**) were not previously considered for pyruvate hyperpolarization. While IMesBn (**1f**), similarly to IBn (**1g**), exhibits poor performance in ^{13}C C$_1$ pyruvate hyperpolarization, IPr (**1b**) and SIPr (**1c**) perform on par, within 20%, with IMes (**1a**) which remains the benchmark catalyst for pyruvate (see Fig. 1b). The NMR spectrum of hyperpolarized [1-^{13}C]pyruvate in methanol-d$_4$ features three distinct peaks corresponding to **4** free pyruvate (~170 ppm in the blue-framed box in Fig. 1a), **3b** bound

Scheme 1 Pyruvate hyperpolarization by SABRE. Free pyruvate is obtained as a reversible process *via* [Ir(H)$_2$(κ^2-pyruvate)(DMSO)(NHC)] (**3**), whereas hydrogen exchange is mediated by ([IrCl(H)$_2$(DMSO)$_2$(NHC)]) (**2**) as detailed by Duckett *et al.* in ref. 51.

22926 | *Phys. Chem. Chem. Phys.*, 2025, **27**, 22924–22936

This journal is © the Owner Societies 2025

pyruvate (~ 168.7 ppm in the green-framed box in Fig. 1a) and **3a** bound pyruvate (~ 165.4 ppm in the red-framed box in Fig. 1a).

SABRE-SHEATH[22,29,32] hyperpolarized ^{13}C spectra of [1-^{13}C]pyruvate in methanol-d_4 are shown in Fig. 1b for the examined catalysts. They were acquired with bubbling times much longer than the build-up times (see Table SI-2) at 280 K to effectively compare their performance. Following bubbling at 0.33 μT (see Fig. SI-17), the NMR sample tube was manually transferred in ~ 3 seconds to a 1.4 T benchtop NMR spectrometer (Oxford Instruments XPulse), where a carbon 90° pulse was applied for signal acquisition. The results reveal striking differences in catalyst performance, reinforcing the motivation behind this study. Among the tested catalysts, IMes (**1a**), IPr (**1b**) and SIPr (**1c**) emerge as the most effective. IMes (**1a**) achieves more than 3% ^{13}C polarization for free pyruvate, while IPr (**1b**) and SIPr (**1c**), yield a polarization value of $\sim 2.5\%$. In the case of IMes (**1a**), the free and the two bound forms are clearly distinguishable, whereas for IPr (**1b**) and SIPr (**1c**), the majority of the ^{13}C signal is distributed between the free and equatorially bound forms, with only a faint signal corresponding to the axially bound form at 280 K. SIMes (**1d**) shows a somehow reduced performance as compared to the unsaturated counterpart IMes (**1a**), with a ^{13}C polarisation level for free pyruvate of about $\sim 1\%$. IMesCl$_2$ (**1e**), previously investigated for [1,2-^{13}C]pyruvate hyperpolarization,[41] confirms its lower efficiency, yielding $\sim 0.5\%$ polarization for free pyruvate, significantly lower than IMes (**1a**) and IPr (**1b**). The IMesBn (**1f**) and IBn (**1g**) exhibit the weakest performances, with a ^{13}C polarization of approximately 0.02%, more than two orders of magnitude lower than that achieved with IMes (**1a**) and IPr (**1b**).

The persistence of the forms **3a** and **3b** in the spectra of IMes (**1a**) and IPr (**1b**) suggests relatively slow exchange dynamics. SIMes (**1d**) and SIPr (**1c**), the saturated analogues of IMes (**1a**) and IPr (**1b**), act as stronger σ-donors toward the Ir center due to the absence of aromatic stabilization in their imidazolidine rings. This increased electron density at the Ir centre, as evidenced by the large change in the chemical shift of the diagnostic carbene ^{13}C (from 180.9 ppm for IMes to 207.4 ppm for SIMes, and from 182.6 ppm for IPr to 209.4 ppm for SIPr; see SI-3), could result in a slightly weaker bond with the pyruvate ligand, thus increasing the exchange dynamics. This is also reflected in the temperature-dependent polarization profiles, where the optimal polarization temperature for SIPr (**1c**) and SIMes (**1d**) is 5–10 K lower than IPr (**1b**) and IMes (**1a**) (see SI-5 and Fig. SI-16). For IMesCl$_2$ (**1e**), the predominance of the **3b** species has been already rationalised because of the electron-withdrawing Cl substituents on the NHC ligand, which increase metal centre electron deficiency, strengthening pyruvate binding and further slowing ligand exchange. For IMesBn (**1f**) and IBn (**1g**), the reduced polarization efficiency may stem from the steric hindrance imparted by the benzyl rings. Although the enhanced electron-donating character of the NHC ligand—associated with the presence of at least one alkyl substituent on the nitrogen-containing heterocycle—is not clearly reflected in the ^{13}C chemical shift of the carbene carbon in CDCl$_3$ (see SI-3), it could still contribute to lowering the overall carbon polarization efficiency for pyruvate in this class of catalysts.

^{13}C polarization temperature dependence

All spectra in Fig. 1 were acquired at 280 K. However, it is expected that temperature plays a pivotal role in SABRE exchange dynamics.[28,29] Hence, we have systematically investigated the carbon hyperpolarization of [1-^{13}C]pyruvate for all proposed catalysts as a function of temperature (see SI-5 and Fig. SI-16). Fig. 2 shows the integrated ^{13}C signal areas of free pyruvate and **3b** (blue and green bars respectively) over the 240–310 K temperature range for catalysts **1a**, **1b**, and **1e** after 25 s parahydrogen bubbling at 6 bars. These catalysts represent two classes of NHCs with different electron densities at the metal center and display up to a tenfold difference in free pyruvate hyperpolarization, making them suitable to test the theoretical model described below. For completeness, all temperature profiles and the ^{13}C spectra after 25 s parahydrogen bubbling, 6 bars and 280 K are provided in Fig. SI-16.

The set of experimental NMR processing parameters used for the temperature profile data like receiver gain, number of digitization points, pulse duration, spectral width and acquisition time are identical for all experiments. Note that, unlike the spectra in Fig. 1, all the temperature profiles were acquired with a 25 s bubbling time.

All the examined catalysts show some common traits. The free and bound pyruvate signals (when detected) starting from low values at 240 K reach a maximum in ^{13}C signal intensity at an intermediate temperature around 270–290 K and then decay to zero above 310 K. However, in IPr (**1b**) and SIPr (**1c**), the signal from **3a** is much less intense as compared to IMes (**1a**) across the entire temperature range and at the optimal free pyruvate temperature, 280 K, the **3a** signal is barely visible. Overall, the optimal **3b** temperature for the examined catalysts ranges from about 260.0 K and 285.0 K, slightly higher than the optimal **3a** temperature, whereas the optimal free pyruvate temperature is observed within 270 K and 290 K. These different peak temperatures point clearly to different dynamic regimes for free pyruvate, **3b** and **3a**.

Due to the ~ 5 K gap between the optimal temperatures for the **3b** and free pyruvate signals, the temperature that yields the highest overall signal intensity falls in between (brown bar in Fig. 2 and Fig. SI-16). It ranges from 270.0 K to 285 K.

The bell-shaped curve for all the catalysts demonstrates that one can modulate the binding affinity between the pyruvate and the catalyst by changing the temperature. At low temperatures the relatively higher **3b** signal intensity, indicates a strong binding mode and a slow exchange regime. Temperatures above 280 K, in contrast, are consistent with a weaker binding mode and a faster exchange regime for IMes (**1a**) and IPr (**1b**) as highlighted by the relatively higher blue signal intensity in Fig. 2. Remarkably, for IMesCl$_2$ (**1e**), the **3b** peak is instead the strongest across the entire temperature range. The corresponding strong binding affinity and weak exchange regime become detrimental for an efficient free pyruvate hyperpolarization.

This journal is © the Owner Societies 2025

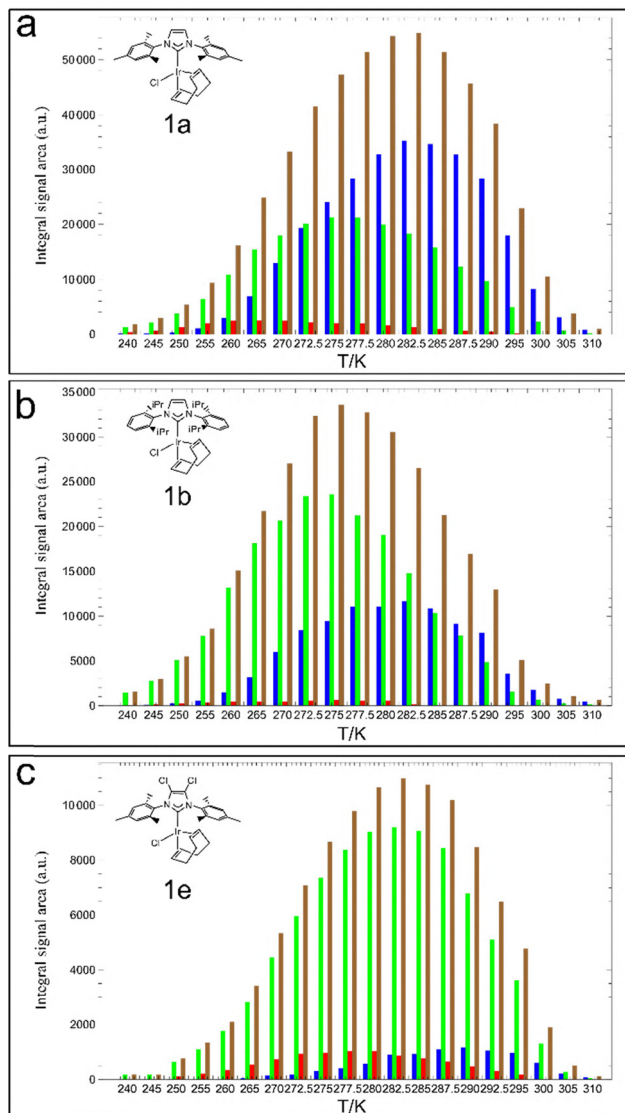Phys. Chem. Chem. Phys., 2025, **27**, 22924–22936 | **22927**

Fig. 2 Bar charts representing experimental data for the variable temperature experiments in (a) for IMes (**1a**), in (b) for IPr (**1b**) and in (c) for IMesCl$_2$ (**1e**). Bars in blue for free pyruvate, in green for the equatorial bound form **3b** and in red for the bound form **3a**, according to the nomenclature in Scheme 1. The brown bar is the sum of the integrated signal areas for **3b**, **3a** and free pyruvate at each temperature. The variable temperature experiments were acquired in all cases with a bubbling time of 25 s with 6 mM catalyst, 30 mM DMSO and 20 mM sodium [1-^{13}C]pyruvate in 700 μL methanol-d$_4$. Additional bar charts are in SI-5 in Fig. SI-16.

This can be explained by the low electron density at the metal center due to the presence of Cl atoms.[41]

The form **3b**, as expected, is the dominant bound form for all the catalysts. It is about 40 times more intense than **3a** (when **3a** was detected) for IPr (**1b**), up to about 25 times higher for IMes (**1a**) (when **3a** was detected), 5–20 for IMesCl$_2$ (**1e**), whereas for IMesBn (**1f**) and IBn (**1g**) the low polarization level did not allow us to identify any signal from **3a**.

Furthermore, while the **3b**/free pyruvate intensity ratio remains around 1 ± 0.5 at the optimal free pyruvate temperature

for **1a**–**1d** and **1g**, it rises significantly to 5.7 for **1e** at 290 K, confirming this catalyst's strong binding affinity.

Among all the examined catalysts, IMes (**1a**), IPr (**1b**) and SIPr (**1c**) stand out, delivering the highest **3b**, free pyruvate, and overall ^{13}C polarization. The key distinction between IMes (**1a**) and IPr (**1b**)/SIPr (**1c**) lies in the **3a** form, which appears significantly less prominent in IPr (**1b**) and SIPr (**1c**) compared to IMes (**1a**). The lower intensity of **3a** in IPr (**1b**) could be related to impaired exchange dynamics, possibly due to the increased steric hindrance induced by the isopropyl groups. However, further investigations are needed to fully support this hypothesis.

Since NMR signal amplification—whether achieved through PHIP, SABRE, CIDNP, or DNP—is inherently a non-equilibrium process, we explored a dynamic temperature approach in addition to the fixed-temperature hyperpolarization experiments shown in Fig. SI-16 and Fig. 2. In this method, the sample is first equilibrated at 265 K before gradually increasing the temperature to 280 K during the 25 s-long hydrogen bubbling, after which the signal is acquired at 1.4 T. The experiment is then repeated with the temperature change in the opposite direction from 285 K to 265 K (Fig. SI-20).

In this modality, the bubbling that mediates polarization transfer takes place under non-equilibrium conditions, as the temperature changes over the 25-second bubbling period. We found that increasing the temperature during bubbling led to a consistent ~50% drop in free pyruvate signal intensity compared to acquisition at 280 K bubbling temperature. Conversely, ramping the temperature down during bubbling resulted in only a modest ~3% gain in free pyruvate signal intensity. Ramping up or down the temperature does not seem to impact drastically the signal intensity of **3a** and **3b**. The data include two to three replicates per condition. Three representative spectra stacked horizontally are presented in Fig. SI-20.

DMSO and parahydrogen pressure dependence of the ^{13}C polarization at variable temperatures

In addition, the concentration of the sulfoxide co-ligand, here dimethylsulfoxide (DMSO), plays a crucial role in modulating the equilibrium between the equatorial (**3b**) and axial (**3a**) bound forms of pyruvate in SABRE hyperpolarization. By increasing the DMSO equivalents from 3 to 20, we observe a decrease in the population of the equatorial form (**3b**) and a corresponding increase in the axial form (**3a**) for both IMes (**1a**) and IPr (**1b**) catalysts across the temperature range of 240–310 K (see Fig. SI-18). This behavior is in line with the observation that DMSO competes with pyruvate for coordination at the equatorial sites, progressively displacing it as its concentration rises. The DMSO competition is less pronounced for the axially coordinated pyruvate. Consequently, this leads to an accumulation of **3a** in solution and to its higher population with an increasing DMSO amount (see Fig. SI-18).

Interestingly, despite these significant changes in the bound species distribution, while the signal of free pyruvate seems to peak at 5 DMSO equivalent for IMes (**1a**), it remains instead relatively unchanged for IPr (**1b**). This observation implies that

22928 | *Phys. Chem. Chem. Phys.*, 2025, **27**, 22924–22936

This journal is © the Owner Societies 2025

the overall exchange dynamics between bound and free forms remain balanced across the investigated DMSO concentrations (see Fig. SI-18).

In addition, in SI-8 and Fig. SI-21 we report for IMes (**1a**) a variable temperature analysis at 5 DMSO equivalent for different parahydrogen pressures (2, 4 and 6 bars) showing that, as expected, optimal signals are achieved at 6 bars for **3b** and free pyruvate.

Build up time of the ^{13}C polarization at variable temperatures

We measured the build-up time of ^{13}C polarization for the **3a** (in some cases), **3b**, and free pyruvate forms of IMes (**1a**) and

$$
\begin{cases}
\dfrac{d\hat{\rho}_{H_2}}{dt} = \left(\hat{L}_{H_2} - \left(W_{out} + k_{ex}[B_{H_2}]\right)\hat{\mathbb{1}}_{H_2}\right)\hat{\rho}_{H_2} \\
\qquad\qquad + k_{ex}[B_{H_2}]\hat{\rho}_{B_{H_2}} + W_{out}\hat{\rho}^*_{H_2} \\[6pt]
\dfrac{d\hat{\rho}_{B_{H_2}}}{dt} = \left(\hat{L}_{B_{H_2}} - \left(k_{ex}[H_2] + k_{aE}[S] + k_{aA}[S]\right)\hat{\mathbb{1}}_{B_{H_2}}\right)\hat{\rho}_{B_{H_2}} \\
\qquad\qquad + k_{ex}[H_2]\hat{\rho}_{H_2} + k_{aE}[S]\widehat{\widehat{Tr}}_S(\hat{\rho}_{B_E}) + k_{aA}[S]\widehat{\widehat{Tr}}_S(\hat{\rho}_{B_A}) \\[6pt]
\dfrac{d\hat{\rho}_{B_E}}{dt} = \left(\hat{L}_{B_E} - k_{dE}\hat{\mathbb{1}}_{B_E}\right)\hat{\rho}_{B_E} + k_{dE}\hat{\rho}_{B_{H_2}} \otimes \hat{\rho}_S \\[6pt]
\dfrac{d\hat{\rho}_{B_A}}{dt} = \left(\hat{L}_{B_A} - k_{dA}\hat{\mathbb{1}}_{B_A}\right)\hat{\rho}_{B_A} + k_{dA}\hat{\rho}_{B_{H_2}} \otimes \hat{\rho}_S \\[6pt]
\dfrac{d\hat{\rho}_S}{dt} = \left(\hat{L}_S - \left(k_{aE}[B_{H_2}] + k_{aA}[B_A]\right)\hat{\mathbb{1}}_S\right)\hat{\rho}_S \\
\qquad\qquad + [B_{H_2}]\left(k_{aE}\widehat{\widehat{Tr}}_{H_2}(\hat{\rho}_{B_E}) + k_{aA}\widehat{\widehat{Tr}}_{H_2}(\hat{\rho}_{B_A})\right)
\end{cases}
$$

$$(1)$$

IPr (**1b**) at 240 K, 260 K, 280 K, and 300 K and for the others at 280 K (see SI-8 and Fig. SI-19).

At 240 K, the free pyruvate signal was not detected, and we could only estimate the buildup times for **3a** and **3b**.

At 260 K, the free pyruvate signal became detectable, although its buildup remained slow: 23.2 ± 2.5 s for IMes (**1a**) and 15.6 ± 1.8 s for IPr (**1b**).

At 280 K, the free pyruvate build-up time for IMes (**1a**) is 8.2 ± 1.0 s, whereas for IPr (**1b**) it is 18.6 ± 1.3 s, about a factor of two longer. SIPr (**1c**) is characterized by a relatively slow build-up for both **3b** (16.6 ± 3.0 s) and free pyruvate (33.8 ± 3.8 s), whereas SIMes (**1d**) shows a shorter build-up time for **3b** (5.5 ± 0.9 s), which is approximately in line with all other catalysts. The build-up time for free pyruvate with SIMes (**1d**) is also comparable to the others (17.7 ± 2.0 s). For IMesCl$_2$ (**1e**) the buildup times of **3a** (4.3 ± 1.2 s) and **3b** (3.6 ± 1.1 s) are like those found in IMes (**1a**), however the free pyruvate buildup is about a factor of 2 longer than and similar to IPr (**1b**) (16.9 ± 2.2 s). For IBn (**1g**) the build-up times are 3.8 ± 1.0 s and 21.9 ± 2.7 s for **3b** and free pyruvate respectively.

At 300 K, only **3b** and free pyruvate remain visible. In this case, while the buildup time of free pyruvate in IMes (**1a**) is 9.3 ± 2.0 s, for IPr (**1b**), it increases significantly to 35.5 ± 0.8 s.

The data point to a slower pyruvate exchange dynamics in IPr (**1b**), SIPr (**1c**), SIMes (**1d**), IMesCl$_2$ (**1e**), and IBn (**1g**) compared to IMes (**1a**), which directly limits the hyperpolarization

efficiency. However, the reason for these different buildups could vary: for IMesCl$_2$ (**1e**) linked to a reduced electronic density at the metal center, while for IPr (**1b**), and others, due to a more hindered pyruvate exchange dynamic. Consistently with previous considerations, the reduced electronic density for IMesCl$_2$ (**1e**) favors a stronger binding leading to the shortest build-up time for the **3b** form in the series. The build-up times of carbon polarization for **3b** and free pyruvate are among the key factors influencing the ^{13}C polarization trend shown in Fig. 1b. From an experimental standpoint, these times reflect the combined effects of exchange and relaxation rates at a given temperature. In Table SI-3, we summarize all the build-up measurements by introducing a parameter which is the ratio T_b (**3b**)/T_b (free pyruvate). This ratio generally correlates with the observed levels of carbon polarization, with a deviation for SIPr (**1c**), whose build-up times are however associated with a larger experimental uncertainty. All buildups are reported in Section SI-8 in Tables SI-2 and SI-3.

Natural abundance ^{13}C experiments

Finally, despite the parahydrogen enrichment being only 50%, the signal amplification is sufficiently high to allow natural abundance pyruvate experiments to be conducted in a single scan for IMes (**1a**) and IPr (**1b**) (see also ref. 70 and Fig. SI-22). Both free and bound forms at the C$_1$ and C$_2$ positions are detected.

Theory

Several studies have examined the theoretical foundation underlying the SABRE phenomenon. The seminal work of Adams *et al.* first highlighted both the predictability and complexity of nuclear spin hyperpolarization,[71] while Ivanov further emphasized the critical role of level anti-crossing (LAC) effects.[72,73] However, even from the data examined here, it is apparent the dominant role of exchange dynamics, as compared to coherent and incoherent spin evolutions, in SABRE hyperpolarization. Knecht *et al.* introduced an explicit treatment of chemical exchange,[74] which was further expanded in the comprehensive chemical and physical (CAP) model developed by Pravdivtsev *et al.*[50] The CAP model represents one of the most detailed and systematic frameworks, specifically in describing the hyperpolarization of N-donor substrates such as pyridine. It treats the spin dynamics of SABRE as a direct exchange of hydrogen and substrate directly over the bound states of the Ir catalyst. Although such model is suitable for N-donors substrates, it is not accurate in the case of pyruvate, where the hydrogen exchange is not mediated by the bound forms $[Ir(H)_2(\kappa^2\text{-pyruvate})(DMSO)(NHC)]$ (**3a** and **3b**), but by the intermediate $[IrCl(H)_2(DMSO)_2(NHC)]$ (**2**), as reported by Duckett and co-workers[41,51] and illustrated in Scheme 1.

In this work, we model the SABRE of pyruvate as a two-step exchange at the iridium centre as per Scheme 1. In the first step, hydrogen is exchanged at the intermediate **2** (B_{H_2} in the equations below).[41,51,75] In the second step, the chloride anion

This journal is © the Owner Societies 2025

Phys. Chem. Chem. Phys., 2025, **27**, 22924–22936 | **22929**

(green circle in Scheme 1) and one DMSO molecule (brown circle in Scheme 1) are ejected ("−" sign in Scheme 1) to allow pyruvate (red circle in Scheme 1) to bind in a bidentate fashion, either equatorially in **3b** (B_E in the equations below) or axially in **3a** (B_A in the equations below). NMR spectroscopy and DFT calculations[41,51] provide strong evidence that, among all possible conformers, the configuration in which pyruvate and hydrides adopt equatorial positions while DMSO is bound axially is energetically favoured and the most realized in solution. The signal of this form is represented by the green bars in Fig. 2 and Fig. SI-16.

In analogy with the prescription used to formulate the CAP model of the SABRE in pyridine we introduce the system of differential equations, eqn (1). The set of equations describes the spin dynamics and chemical exchange for each substrate taking part in the SABRE process. The first equation describes the evolution of free hydrogen, and the second equation refers explicitly to the intermediate [IrCl(H)$_2$(DMSO)$_2$(NHC)] (**2**) introduced above. It was not present in the original CAP model as, for pyridine, the hydrogen exchanges directly on the bound substrate without the presence of intermediates. The last three equations describe the evolution of the spin system in the equatorial and axial bound systems and free substrate (pyruvate), respectively.

In the equations, $\widehat{\widehat{L}}$ and $\widehat{\widehat{1}}$ represent the Liouvillian and identity superoperators respectively. The tensor product $\otimes$ is involved in the association steps and the partial trace superoperator over the degree of freedom of the released subsystem (Tr$_{sub}$) is involved in the dissociation steps of the exchange processes. Dissociation and associations also act as a dampening factor for the evolution of the density matrix of the involved spin system. $\hat{\rho}^*_{H_2}$ is the density operator of the para-enriched hydrogen gas continuously delivered from a parahydrogen generator (or storage canister) and the source of the spin polarization:

$$\hat{\rho}^*_{H_2} = \frac{\hat{1}_{H_2}}{4} - \frac{4f-1}{3}\hat{I}_1 \cdot \hat{I}_2 \qquad (2)$$

where f is the para-enrichment fraction. The concentrations $[B_{H_2}]$, $[B_A]$, $[B_E]$ and $[S]$, corresponding to those of **2**, **3a**, **3b** and **4** in Scheme 1, can be expressed in terms of catalyst and substrate concentrations at the preparation stage and in terms of the exchange constants (k_{aA}, k_{dA}, k_{aE}, k_{dE}, k_{ex}), see the SI for details.

To achieve SABRE, the hydrogen gas has to penetrate in the solution and dissolve at the molecular level. Under moderate bubbling conditions, the large interfacial bubble area enhances gas to liquid transfer. In small liquid volumes, efficient mixing effects, due to bubble motion, allow to reach rapidly a homogenous equilibrium situation and the concentration of hydrogen in the liquid is assumed to follow Henry's law:

$$[H_2] = k_H P \qquad (3)$$

where k_H is Henry's constant, whose temperature dependence is reported in the SI. The rate of H_2 replacement in the liquid is:

$$W_{out} = \frac{Q}{k_H R T V_L + V_G} \qquad (4)$$

where Q is the volumetric gas flow, P and T are the pressure and the absolute temperature, R is the perfect gas constant and V_L and V_G are the effective volumes of liquid and gas phase during the bubbling, respectively (see SI-11.2).

In essence, the model distils the complex physics and chemistry of SABRE into effective exchange rates, which are influenced by both experimental parameters and molecular interactions.

Description of the model

As for the quantum mechanical part of the system of equations, eqn (1), several spin systems can be recognized. Two hydrogens for free H_2 and two hydrides for **2** (B_{H_2}); two hydrides, one ^{13}C in C_1, and three methyl ^1H for each bound **3a** (B_A) and **3b** (B_E) forms; one ^{13}C in C_1, and three methyl ^1H for free pyruvate (S). Incorporating in the model the methyl protons enable a more accurate description of pyruvate relaxation without relying on random field approximations as for the CAP, or phenomenological relaxation times.[50] At low magnetic fields, relaxation is primarily driven by intramolecular dipolar interactions, which depend on the molecular geometry (internuclear distances and torsional angles) and rotational correlation times. We used DFT calculations (see SI-DFT) to determine the chemical shifts, J-coupling network, and molecular structures of all species involved in the SABRE process for pyruvate, extending previous works which concentrated on evaluating the chemical shifts of the hydrides Ir–IMes complex with different functionals and level of theory and few relevant J-coupling for the relevant SABRE complex [Ir(H)$_2$(κ^2-pyruvate)(DMSO)(IMes)].[67,69] Here we obtained a better agreement between calculated and experimental J-coupling constants[69] likely due to the use of a larger basis set in the context of two-component relativistic DFT calculations. Notably, in terms of spin dynamics, the only free parameters in our model are the correlation times, which directly influence the incoherent part of the Liouvillian and consequently the relaxation rates. It is important to note that the structural variations among all the catalysts from **1a** to **1g** are not conducive to drastically different J-coupling values in the bound complexes according to our calculations (see Table SI-DFT), underscoring the critical role of exchange rates—under identical flow, concentration, pressure, and temperature conditions—in accurately interpreting SABRE experiments. The system in eqn (1) in full form is highly demanding to treat numerically because of the large dimensionality of the Liouville spaces involved (2^{2N} for an N spin-1/2 spin system). To reduce the computational effort, we observe that the evolution superoperators preserve the total z-spin quantum number and are symmetric for exchange of the methyl protons (assuming unhindered rotational freedom in the liquid state). It follows that in the system of equations above, the analysis of the spin dynamics can be restricted to the zero-quantum operator basis, symmetrized with respect to exchange of the methyl protons operators. Hence the dimensionality of the problem is reduced according to the following:

- 6 operators for free H_2 and for the bound case C (rather than 16): $\hat{1}_{H_2}$, $\hat{S}_{1z} + \hat{S}_{2z}$, $\hat{S}_{1z} - \hat{S}_{2z}$, $T_{00}(\hat{S}_1,\hat{S}_2)$, $T_{10}(\hat{S}_1,\hat{S}_2)$, $T_{20}(\hat{S}_1,\hat{S}_2)$

22930 | *Phys. Chem. Chem. Phys.*, 2025, **27**, 22924–22936

This journal is © the Owner Societies 2025

- 20 operators for free ^{13}C-labelled pyruvate (rather than 64):
- 266 operators (rather than 4096) for any bound H_2 and ^{13}C-labelled species.

The parameters under experimental control are the temperature T, the pressure P and the volumetric flow Q. The flow is measured by a gas flowmeter (Sierra Instruments model C100M).

To match experimental conditions, the following parameters/conditions have been used: the Ir catalyst concentration $[\text{IrCat}]_0$ is 6 mM; pyruvate concentration $[S]_0$ is 20 mM and we assume that at the initial time the catalyst is in the activated state. The bubbling pressure P = 6 bar and the concentration of free hydrogen in the liquid phase is derived from Henry's law, eqn (3). Following the discussion in the SI, the H_2 concentration varies almost linearly with pressure and temperature. For example, at pressure of 6 bar $[H_2]$ goes from ~ 15 mM at 240 K up to ~ 29 mM at 310 K. The parahydrogen volumetric flow Q is set to 80 sccm. We assume that bubbling is very effective in exchanging fresh parahydrogen locally into the liquid and we use eqn (4) with an effective gas value of V_G = 0 and Henry's law to evaluate the temperature dependence of W_{out}, via eqn (4). It follows that W_{out} decreases monotonically from a value of 38 s^{-1} to 15 s^{-1} when the temperature increases from 240 K to 310 K at a fixed pressure of 6 bar. The parahydrogen fraction f is set at 50% unless explicitly stated otherwise. The initial states are assumed to be the identity density operators in their appropriate spin space.[50]

The solutions of eqn (1) yield four density spin operators $\left(\hat{\rho}_{H_2}, \hat{\rho}_{B_{H_2}}, \hat{\rho}_{B_E}, \hat{\rho}_S \right)$. Each $\hat{\rho}$, is a function of B_0, bubbling time, exchange rates, hydrogen concentration, W_{out}, and correlation times and enables the calculation of all relevant experimental observables. The expectation value for z-magnetization is estimated using the standard formula $\langle \hat{S}_z \rangle = \text{Tr}(\hat{\rho}\hat{S}_z)$ and polarizations are calculated as $P = \langle \hat{S}_z \rangle / 2^{N-1}$ where N is the number of spins $\frac{1}{2}$ in the spin system. Molar polarizations are defined as the product of polarizations by concentration.

In the following, for simplicity we disregard the exchange pathway leading to the axial form (**3a**, B_A) and focus our analysis on the exchange between the hydrogen-bound form B_{H_2} (**2**) and the equatorially bound form (**3b**, B_E). This simplification is justified because the axial exchange pathway has a negligible contribution to the overall exchange process, and experimental as well as theoretical evidence suggests that exchange predominantly occurs through the equatorial configuration.[28,29,33,36,41,51]
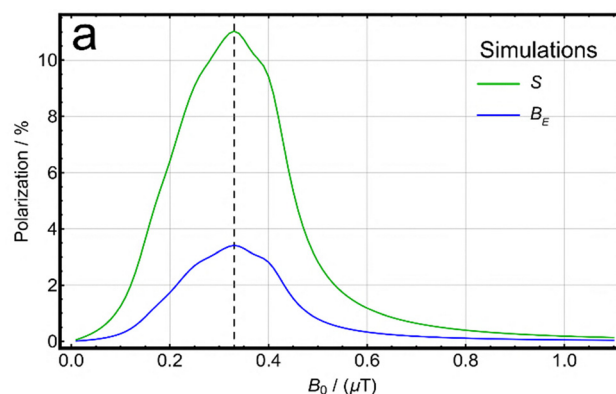
Magnetic field profiles

In SABRE-SHEATH experiments the maximum ^{13}C polarization for [1-^{13}C]pyruvate occurs when the parahydrogen is supplied at the magnetic field matching the condition $|B_0| = 2\pi \dfrac{|J_{HH}|}{|\gamma_{^1H} - \gamma_{^{13}C}|}$, where J_{HH} is the hydride J-coupling in the bound states and γ are the nuclear gyromagnetic ratios.[23,76] In SI-3 we report, as an example, the experimental magnetic field profiles for **1a** and **1e**, and indeed the maximum signal transfer occurs at around

0.33 μT for both catalysts in line with our DFT findings of no major change in J-coupling between different catalysts (see SI-DFT). Fig. 3 shows simulated polarization field profiles for bound ($\langle \hat{B}_{E,z} \rangle$) and free pyruvate ($\langle \hat{S}_z \rangle$) based on J-couplings and optimized geometry of IMes (**1a**) complex after 25 s of hydrogen bubbling at T = 280 K, with $[H_2]$ = 21.9 mM and W_{out} = 22.5 s^{-1}, within the magnetic field range 0.1–1.1 μT. The rates were set to k_{aE} = 10 M^{-1} s^{-1}, k_{dE} = 0.2 s^{-1}, and k_{ex} = 10 M^{-1} s^{-1}. In the following, we fixed the values for the rotational correlation times: τ_{H_2} = 0.4 ps, τ_S = 100 ps, $\tau_{B_{H_2}} = \tau_{BE}$ = 180 ps. Such choice of rates and correlation times was informed by the analysis of the temperature-dependent SABRE experiments detailed below (see Fig. 2 and also Fig. SI-16). These values were chosen so that the simulated polarization and signal profiles for the equatorially bound and free pyruvate forms could match the corresponding experimental profiles in the case of the IMes (**1a**) catalyst. In particular, the rates correspond to the values expected at around T = 280 K (the maximum observed signal in free pyruvate) following the fitting of the experimental temperature dependence with the theoretical model, see (Fig. 5). Further details are provided in the SI.

The field profiles exhibit a peak at approximately 0.33 μT, with a FWHM of ~ 0.3 μT slightly skewed toward higher fields, consistent with experimental observations. A more detailed analysis of the dependence of the field profiles and build-up times is given in SI-11.3 and SI-11.4. Crucially, the symmetry considerations outlined above enabled a substantial reduction in the computational resources needed for the simulations, consistently reducing computation time. For example, the field profile simulation time was cut to one third of that required by a full-space approach.

^{13}C$_1$ polarization dependence on W_{out}, k_{ex} and $[H_2]$

We have then examined the effect of W_{out}, hydrogen concentration $[H_2]$ and exchange rates on the ^{13}C$_1$ polarizations at 0.33 μT. Fig. 4 shows that W_{out} does not affect polarization

Fig. 3 (a) Simulated field profile for the ^{13}C$_1$ polarization levels based on J-couplings and optimized geometry of IMes (**1a**) complex for free pyruvate (S) and equatorially bound pyruvate (B$_E$) after 25 s bubbling with 50% *para*-enriched hydrogen at k_{aE} = 10 M^{-1} s^{-1}, k_{dE} = 0.2 s^{-1}, k_{ex} = 10 M^{-1} s^{-1}, $[H_2]$ = 21.9 mM and W_{out} = 22.5 s^{-1}. The vertical dashed line marks 0.33 μT.

This journal is © the Owner Societies 2025
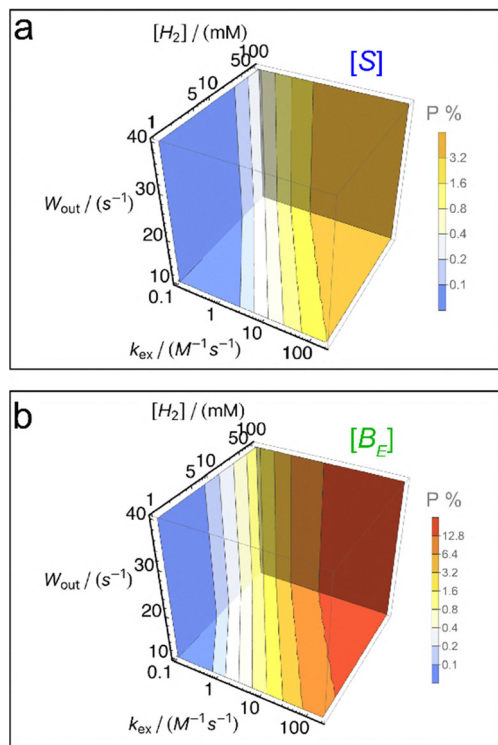
Phys. Chem. Chem. Phys., 2025, **27**, 22924–22936 | **22931**

Fig. 4 Simulated dependence of the $^{13}C_1$ spin polarizations at 0.33 μT in (a) for free pyruvate (S) and (b) for equatorially bound pyruvate B_E in function of k_{ex}, [H_2] and W_{out} at $k_{aE} = 10$ M^{-1} s^{-1}, $k_{dE} = 0.2$ s^{-1} after bubbling for 25 s with 50% *para*-enriched hydrogen.

levels within in the region relevant for our experiments, namely 15 s$^{-1} \leq W_{out} \leq 40$ s^{-1}. This can be explained by noting that when $W_{out} \gg k_{ex}[B_{H_2}]$, the term $k_{ex}[B_{H_2}]$ becomes negligible in the system's first differential equation. This has two key implications: (i) the para-subspace projection of the free hydrogen density matrix, $\hat{\rho}_{H_2}$, equilibrates on a timescale set by $1/W_{out}$; (ii) spin dynamics depend not on k_{ex} and [H_2] individually, but on their product $k_{ex}[H_2]$, as apparent from the equations. Fig. 4 supports these observations, showing polarization levels aligned along anti-diagonal stripes in the $\log k_{ex} - \log[H_2]$ plane. In all the simulations, we have constrained $k_{ex} \leq 210$ [M^{-1}] s^{-1}. Given the initial experimental preparation, $[B_{H_2}] \leq 6$ mM, the condition $W_{out} \geq 15$ s$^{-1} \gg k_{ex}[B_{H_2}] \geq 1.2$ s^{-1} is always satisfied. It is worth noting that beyond a certain value of the exchange rate $k_{ex}[H_2] \sim 0.2$ s^{-1}, the polarization approaches an asymptotic limit, reflecting the fact that above a certain threshold fresh hydrogen is exchanging so rapidly from the gas phase that in the bound form **2** the hydrides are in the same spin state of the gas phase, which determines the limit on induced polarization levels.

Simulations of the temperature dependence of the hyperpolarized signals and comparison with experiments

SABRE-SHEATH experiments are typically performed at a constant temperature, which corresponds to a single point in the k_a-k_d parameter space. The spectra in the experimental series shown in Fig. 2 and Fig. SI-16 were acquired at different temperatures corresponding to different points in the k_a-k_d space. In Fig. 5a, the experimental data points are shown for free pyruvate **4** (in blue) and bound form **3b** (in green), for IMes (**1a**), IPr (**1b**), and IMesCl$_2$ (**1e**) catalysts. The blue and green lines represent the best-fit of the experimental data to the model described in eqn (1) assuming an exponential relation between rates and temperatures at fixed correlation times $\tau_{H_2} = 0.4$ ps, $\tau_S = 100$ ps, $\tau_{B_{H_2}} = \tau_{BE} = 180$ ps for all the considered catalysts, see SI-11-5.

The top contour plots in Fig. 5b and c display the simulated polarization levels for free pyruvate **4** and bound pyruvate **3b** in the k_a-k_d parameter space, respectively. In addition to the polarizations in Fig. 5b, the contour plots in Fig. 5c also show the molar polarization contour plots. Molar polarizations directly correlate to the intensity of the observed NMR signal. In both panels in Fig. 5b and c, the best-fit temperature profiles for IMes (**1a**), IPr (**1b**), and IMesCl$_2$ (**1e**) appear as trajectories— indicated by grey lines—across these parameter landscapes shown as contour plots. Since the system dynamics change with temperature, both polarization and species concentrations are affected. The SABRE catalyst's efficiency can therefore be assessed by identifying the trajectory that overlaps most extensively with regions of high molar polarization.

How should one perform the experiment to achieve maximum signal in the free pyruvate form?

The experiments reported in Fig. 2, SI-5 and Fig. SI-16 highlight the role of temperature on the three detected forms of pyruvate across all examined catalysts.
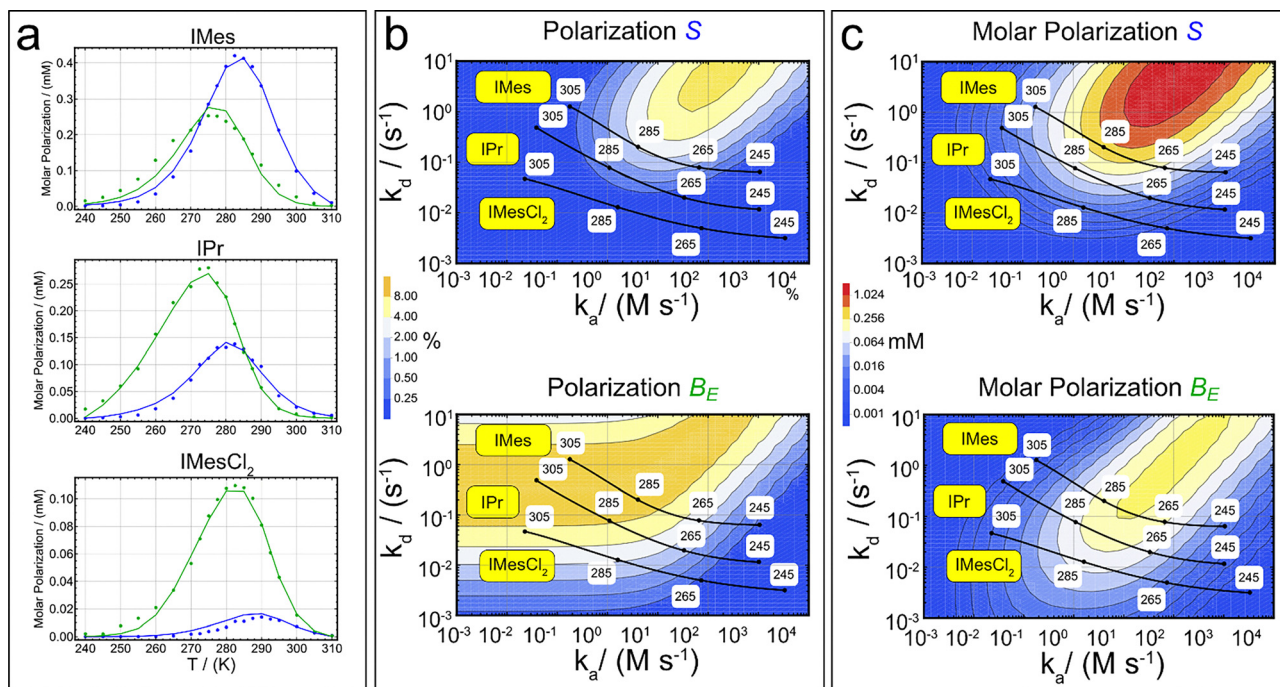
Given that many studies on hyperpolarized pyruvate focus on maximizing the signal of the free form, a natural question arises: can we design an experimental protocol that optimizes the molar polarization of the free species? The experimental observations indicate that in the case of IMes, IPr, SIPr, and SIMes, performing the (para-)hydrogenation at a controlled temperature between 270 K and 280 K enhances the overall ^{13}C signal but does not necessarily favor the free form. Even in cases when the free form is dominant, the signal from the equatorially bound species is not negligible. In some catalysts, the signal from the bound species, despite its lower concentration, exceeds that of free pyruvate (see Fig. SI-16). These observations lead to a further question: is it possible to transfer part of the signal from the catalyst-bound to the free form?

Fig. 6 illustrates a proposed to reach such a goal.

The contour plots in Fig. 6a map the concentrations of **3b** and free pyruvate in the k_a-k_d parameter space. Moving from the bottom right to the top left of the plane, the concentration of the bound form decreases and the concentration of the free from increases. A constant temperature experiment corresponds to a single point within this plane.

Since the total signal for each species is given by the product of concentrations by polarizations, one possible strategy to increase the free molar polarization is: (a) to perform bubbling at the temperature corresponding to the maximum total signal (close to the center of the contour plots) and then (b) move

22932 | *Phys. Chem. Chem. Phys.*, 2025, **27**, 22924–22936

This journal is © the Owner Societies 2025

Fig. 5 (a) Experimental (dots) and fitted data (lines) for the variable temperature experiments in blue for free pyruvate (S) and in green for the equatorial bound form (B$_E$) **3b** for IMes (**1a**), IPr (**1b**) and IMesCl$_2$ (**1e**) using the model in eqn (1). Experiments performed at 6 bar parahydrogen pressure, 25 s bubbling time and 6 mM catalyst, 20 mM [1-^{13}C]pyruvate, 30 mM DMSO in methanol-d$_4$. (b) Contour plots of polarizations and (c) molar polarizations in the k_a–k_d subspace for free pyruvate and **3b** forms. The solid black lines in the contour plots indicate the trajectories of the rates in the variable temperature experiments corresponding to IMes, IPr and IMesCl$_2$ going from top to bottom, respectively.

rapidly in the plane to deplete the **3b** pool in favor of the free pyruvate pool. Graphically, this would correspond to travel along a trajectory in the k_a–k_d space in the direction indicated by the arrow in Fig. 6a. Following the analysis of the temperature-dependent experiments, such strategy corresponds to a rapid temperature increase immediately after stopping the parahydrogen supply, as exemplified by the temperature-jump modality illustrated in Fig. 6b.

In the experimental demonstration of such a procedure, shown in Fig. 6c for IMes (**1a**), concentric magnetic rings were placed inside a Plexiglas cylinder filled with hot water as described in the SI. The bath was not thermally regulated or isolated. The magnetic field inside the ring region was used to reduce the relaxation losses that would otherwise occur at the Earth's magnetic field. After hydrogen bubbling at 280 K for 25 s, the sample was moved in about 2 s from the mu-metal shield into the hot bath at an approximate temperature of 330 K. The sample was kept at such elevated temperature for 5 seconds before being transferred to the benchtop NMR spectrometer for detection. The experiment was performed in three replicates. Representative spectra are reported in Fig. 6c. On average, the free pyruvate peak increased by approximately 32%, while the **3b** peak decreased by 29%. The **3a** resonance disappeared entirely, and a peak corresponding to either the hydrated form of pyruvate or pyruvate dimers emerged. Following the temperature jump approach, rationalized in terms of the analytical framework developed in the previous section, the molar polarization in the free pyruvate increased from about
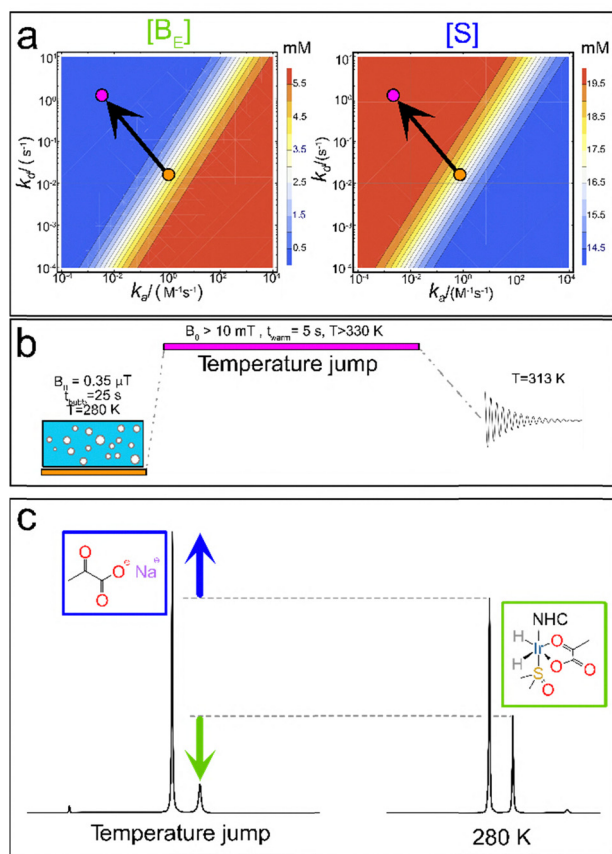
0.42 mM to 0.56 mM. To improve the polarization levels further, several parameters must be carefully optimized, including the magnitude of the temperature jump, the duration the sample remains at elevated temperature (t_{warm}), and the magnetic field experienced by the sample during this phase. More thorough future investigations are warranted. We note that a conceptually related approach has been previously described by TomHon *et al.*, who implemented a temperature cycling strategy to enhance ^{13}C SABRE-SHEATH polarization of pyruvate.[29] In their case, the sample was initially cooled and then allowed to gradually warm up during bubbling, leading to a time-dependent temperature gradient across the sample. In contrast, the temperature jump protocol proposed here involves a thermally equilibrated bubbling phase at constant temperature, of 280 K for IMes (**1a**), followed by a temperature and magnetic field increase applied only after the SABRE polarization step. The ^{13}C NMR detection then occurs on a 60 MHz benchtop spectrometer, approximately 3 seconds after the five-second-long warming period. This methodology ensures well-defined and reproducible thermal conditions during parahydrogen exchange, while providing temporal and thermal separation between the polarization and detection environments.

Conclusions

In this work, we presented an integrated study combining the synthesis and evaluation of seven Ir-based SABRE catalysts, a

This journal is © the Owner Societies 2025

Phys. Chem. Chem. Phys., 2025, **27**, 22924–22936 | **22933**

Fig. 6 (a) Contour plots representing the parameter space defined by the association (k_a) and dissociation (k_d) rate constants. At 280 K, the exchange regime is indicated by the brown filled circle, positioned near the centre of each plot. Upon increasing the temperature, the new kinetic regime is represented by the pink filled circle. (b) Schematic of the temperature-jump experiment: 50% parahydrogen bubbling is performed for 25 s at 280 K in a low magnetic field (~ 0.33 μT), followed by a rapid switch to a higher magnetic field (> 10 mT) and elevated temperature (330 K) for 5 s. The sample is then transferred within 3 s to a 1.4 T detection field at 313 K. (c) Horizontally stacked ^{13}C NMR spectra obtained using 6 mM IMes (**1a**), 20 mM [1-^{13}C]pyruvate, and 30 mM DMSO. The rightmost spectrum corresponds to 25 s bubbling at constant 280 K and 6 bar pressure. The left spectrum was acquired using the temperature–jump modality described in panel (c). Bubbling time and pressure were kept identical in both experiments.

systematic variable-temperature and co-ligand investigation, and the development of an efficient computational framework. Among the catalysts tested, IPr and SIPr emerged as highly effective alternatives to the benchmark IMes, achieving polarization levels within $\sim 20\%$. In contrast, IMesBn and IBn displayed poor performance, yet offered valuable insight into how subtle modifications around the imidazole ring can dramatically alter exchange kinetics and polarization efficiency. Our temperature-dependent experiments confirmed the critical role of exchange dynamics in governing pyruvate hyperpolarization, a conclusion further supported by the theoretical model. By overcoming the dimensionality bottleneck of Liouville-space formalism, the model enables rapid and predictive simulations of the polarization field profile, build-up, polarization levels,

and temperature effects. As a direct application, we devised a novel protocol incorporating a temperature jump to selectively boost the signal of free pyruvate. This approach led to a $\sim 30\%$ increase in the free pyruvate signal mainly at the expense of the equatorially bound form, with room for further improvement. Altogether, this work advances both the mechanistic understanding and practical optimization of SABRE, offering a robust framework to guide future developments in hyperpolarization strategies and catalyst design.

Author contributions

Conflicts of interest

There are no conflicts to declare.

Data availability

The data supporting this article have been included as part of the SI. Supplementary information is available. See DOI: **https://doi.org/10.1039/d5cp01773d**.

NMR data, Mathematica notebook and DFT files for this article are available at Zenodo at **https://doi.org/10.5281/zenodo.17208744**.

CCDC 2445882 contains the supplementary crystallographic data for this paper.[77]

Acknowledgements

22934 | *Phys. Chem. Chem. Phys.*, 2025, **27**, 22924–22936

This journal is © the Owner Societies 2025

Notes and references

1 E. Luchinat, M. Cremonini and L. Banci, *Chem. Rev.*, 2022, **122**, 9267–9306.

2 E. Luchinat and L. Banci, *IUCrJ*, 2017, **4**, 108–118.

3 D. Sakakibara, A. Sasaki, T. Ikeya, J. Hamatsu, T. Hanashima, M. Mishima, M. Yoshimasu, N. Hayashi, T. Mikawa, M. Wälchli, B. O. Smith, M. Shirakawa, P. Güntert and Y. Ito, *Nature*, 2009, **458**, 102–105.

4 J. Eills, D. Budker, S. Cavagnero, E. Y. Chekmenev, S. J. Elliott, S. Jannin, A. Lesage, J. Matysik, T. Meersmann, T. Prisner, J. A. Reimer, H. Yang and I. V. Koptyug, *Chem. Rev.*, 2023, **123**, 1417–1551.

5 T. G. Walker, *J. Phys.: Conf. Ser.*, 2011, **294**, 012001.

6 A. Comment, *J. Magn. Reson.*, 2016, **264**, 39–48.

7 A. Bornet, M. Maucourt, C. Deborde, D. Jacob, J. Milani, B. Vuichoud, X. Ji, J. N. Dumez, A. Moing, G. Bodenhausen, S. Jannin and P. Giraudeau, *Anal. Chem.*, 2016, **88**, 6179–6183.

8 J. B. Hövener, A. N. Pravdivtsev, B. Kidd, C. R. Bowers, S. Glöggler, K. V. Kovtunov, M. Plaumann, R. Katz-Brull, K. Buckenmaier, A. Jerschow, F. Reineri, T. Theis, R. V. Shchepin, S. Wagner, P. Bhattacharya, N. M. Zacharias and E. Y. Chekmenev, *Angew. Chem., Int. Ed.*, 2018, **57**, 11140–11162.

9 S. J. Elliott, Q. Stern, M. Ceillier, T. El Darai, S. F. Cousin, O. Cala and S. Jannin, *Prog. Nucl. Magn. Reson. Spectrosc.*, 2021, **126–127**, 59–100.

10 C. R. Bowers and D. P. Weitekamp, *J. Am. Chem. Soc.*, 1987, **109**, 5541–5542.

11 T. C. Eisenschmid, R. U. Kirss, P. P. Deutsch, S. I. Hommeltoft, R. Eisenberg, J. Bargon, R. G. Lawler and A. L. Balch, *J. Am. Chem. Soc.*, 1987, **109**, 8089–8091.

12 D. Canet, C. Aroulanda, P. Mutzenhardt, S. Aime, R. Gobetto and F. Reineri, *Concepts Magn. Reson., Part A*, 2006, **28A**, 321–330.

13 C. R. Bowers and D. P. Weitekamp, *Phys. Rev. Lett.*, 1986, **57**, 2645–2648.

14 J. Natterer and J. Bargon, *Prog. Nucl. Magn. Reson. Spectrosc.*, 1997, **31**, 293–315.

15 F. Reineri, T. Boi and S. Aime, *Nat. Commun.*, 2015, **6**, 5858.

16 P. Nikolaou, B. M. Goodson and E. Y. Chekmenev, *Chemistry*, 2015, **21**, 3156–3166.

17 A. B. Schmidt, E. Y. Chekmenev, H. De Maissin, P. R. Groß, S. Petersen, L. Nagel, F. Schilling, I. Schwartz, T. Reinheckel, J. Hövener and S. Knecht, *Anal. Sens.*, 2024, **4**, e202400039.

18 J. Kurhanewicz, D. B. Vigneron, K. Brindle, E. Y. Chekmenev, A. Comment, C. H. Cunningham, R. J. Deberardinis, G. G. Green, M. O. Leach, S. S. Rajan, R. R. Rizi, B. D. Ross, W. S. Warren and C. R. Malloy, *Neoplasia*, 2011, **13**, 81–97.

19 G. Stevanato, Y. Ding, S. Mamone, A. P. Jagtap, S. Korchak and S. Glöggler, *J. Am. Chem. Soc.*, 2023, **145**, 5864–5871.

20 R. W. Adams, J. A. Aguilar, K. D. Atkinson, M. J. Cowley, P. I. Elliott, S. B. Duckett, G. G. Green, I. G. Khazal, J. Lopez-Serrano and D. C. Williamson, *Science*, 2009, **323**, 1708–1711.

21 K. D. Atkinson, M. J. Cowley, P. I. P. Elliott, S. B. Duckett, G. G. R. Green, J. Lopez-Serrano and A. C. Whitwood, *J. Am. Chem. Soc.*, 2009, **131**, 13362–13368.

22 M. L. Truong, T. Theis, A. M. Coffey, R. V. Shchepin, K. W. Waddell, F. Shi, B. M. Goodson, W. S. Warren and E. Y. Chekmenev, *J. Phys. Chem. C*, 2015, **119**, 8786–8797.

23 T. Theis, M. L. Truong, A. M. Coffey, R. V. Shchepin, K. W. Waddell, F. Shi, B. M. Goodson, W. S. Warren and E. Y. Chekmenev, *J. Am. Chem. Soc.*, 2015, **137**, 1404–1407.

24 D. A. Barskiy, R. V. Shchepin, A. M. Coffey, T. Theis, W. S. Warren, B. M. Goodson and E. Y. Chekmenev, *J. Am. Chem. Soc.*, 2016, **138**, 8080–8083.

25 J. F. Colell, A. W. Logan, Z. Zhou, R. V. Shchepin, D. A. Barskiy, G. X. Ortiz, Q. Wang, S. J. Malcolmson, E. Y. Chekmenev, W. S. Warren and T. Theis, *J. Phys. Chem. C*, 2017, **121**, 6626–6634.

26 J. R. Lindale, S. L. Eriksson, C. P. N. Tanner, Z. Zhou, J. F. P. Colell, G. Zhang, J. Bae, E. Y. Chekmenev, T. Theis and W. S. Warren, *Nat. Commun.*, 2019, **10**, 395.

27 S. Lehmkuhl, M. Suefke, A. Kentner, Y. F. Yen, B. Blumich, M. S. Rosen, S. Appelt and T. Theis, *J. Chem. Phys.*, 2020, **152**, 184202.

28 I. Adelabu, P. TomHon, M. S. H. Kabir, S. Nantogma, M. Abdulmojeed, I. Mandzhieva, J. Ettedgui, R. E. Swenson, M. C. Krishna, T. Theis, B. M. Goodson and E. Y. Chekmenev, *ChemPhysChem*, 2021, **1–7**.

29 P. TomHon, M. Abdulmojeed, I. Adelabu, S. Nantogma, M. S. H. Kabir, S. Lehmkuhl, E. Y. Chekmenev and T. Theis, *J. Am. Chem. Soc.*, 2022, **144**, 282–287.

30 R. V. Shchepin, D. A. Barskiy, A. M. Coffey, T. Theis, F. Shi, W. S. Warren, B. M. Goodson and E. Y. Chekmenev, *ACS Sens.*, 2016, **1**, 640–644.

31 F. Shi, P. He, Q. A. Best, K. Groome, M. L. Truong, A. M. Coffey, G. Zimay, R. V. Shchepin, K. W. Waddell, E. Y. Chekmenev and B. M. Goodson, *J. Phys. Chem. C*, 2016, **120**, 12149–12156.

32 I. Adelabu, M. R. H. Chowdhury, S. Nantogma, C. Oladun, F. Ahmed, L. Stilgenbauer, M. Sadagurski, T. Theis, B. M. Goodson and E. Y. Chekmenev, *Metabolites*, 2023, **13**, 200.

33 A. Ortmeier, K. MacCulloch, D. A. Barskiy, N. Kempf, J. Z. Myers, R. Körber, A. N. Pravdivtsev, K. Buckenmaier and T. Theis, *J. Magn. Reson. Open*, 2024, **19**, 100149.

34 L. Kaltschnee, A. P. Jagtap, J. McCormick, S. Wagner, L. S. Bouchard, M. Utz, C. Griesinger and S. Glöggler, *Chemistry*, 2019, **25**, 11031–11035.

35 A. N. Pravdivtsev, G. Buntkowsky, S. B. Duckett, I. V. Koptyug and J. Hövener, *Angew. Chem., Int. Ed.*, 2021, **60**, 23496–23507.

This journal is © the Owner Societies 2025

Phys. Chem. Chem. Phys., 2025, **27**, 22924–22936 | **22935**

36 S. J. McBride, K. MacCulloch, P. TomHon, A. Browning, S. Meisel, M. Abdulmojeed, B. M. Goodson, E. Y. Chekmenev and T. Theis, *ChemMedChem*, 2024, e202400378.

37 K. MacCulloch, A. Browning, D. O. Guarin Bedoya, S. J. McBride, M. B. Abdulmojeed, C. Dedesma, B. M. Goodson, M. S. Rosen, E. Y. Chekmenev, Y.-F. Yen, P. TomHon and T. Theis, *J. Magn. Reson. Open*, 2023, **16–17**, 100129.

38 K. V. Kovtunov, E. V. Pokochueva, O. G. Salnikov, S. F. Cousin, D. Kurzbach, B. Vuichoud, S. Jannin, E. Y. Chekmenev, B. M. Goodson, D. A. Barskiy and I. V. Koptyug, *Chem. – Asian J.*, 2018, **13**, 1857–1871.

39 G. L. Wibbels, C. Oladun, T. C. O'Hara, I. Adelabu, J. E. Robinson, F. Ahmed, Z. T. Bender, A. Samoilenko, J. Gyesi, L. M. Kovtunova, O. G. Salnikov, I. V. Koptyug, B. M. Goodson, W. M. Snow, E. Y. Chekmenev and R. V. Shchepin, *Magnetochemistry*, 2025, **11**(80), 1–16.

40 I. Smith, N. Terkildsen, Z. Bender, A. Abdurraheem, S. Nantogma, A. Samoilenko, J. Gyesi, L. M. Kovtunova, O. G. Salnikov, I. V. Koptyug, R. Kircher, D. A. Barskiy, E. Y. Chekmenev and R. V. Shchepin, *Molecules*, 2025, **30**(18).

41 B. J. Tickner, O. Semenova, W. Iali, P. J. Rayner, A. C. Whitwood and S. B. Duckett, *Catal. Sci. Technol.*, 2020, **10**, 1343–1355.

42 T. Theis, M. Truong, A. M. Coffey, E. Y. Chekmenev and W. S. Warren, *J. Magn. Reson.*, 2014, **248**, 23–26.

43 S. S. Roy, G. Stevanato, P. J. Rayner and S. B. Duckett, *J. Magn. Reson.*, 2017, **285**, 55–60.

44 A. N. Pravdivtsev, K. Buckenmaier, N. Kempf, G. Stevanato, K. Scheffler, J. Engelmann, M. Plaumann, R. Koerber, J.-B. Hövener and T. Theis, *J. Phys. Chem. C*, 2023, **127**, 6744–6753.

45 V. P. Kozinenko, A. S. Kiryutin and A. V. Yurkovskaya, *Chem.: Methods*, 2025, e202400060.

46 N. Kempf, R. Körber, M. Plaumann, A. N. Pravdivtsev, J. Engelmann, J. Boldt, K. Scheffler, T. Theis and K. Buckenmaier, *Sci. Rep.*, 2024, **14**, 4468.

47 S. Nantogma, S. L. Eriksson, T. Theis, W. S. Warren, B. M. Goodson and E. Y. Chekmenev, *J. Magn. Reson. Open*, 2025, **24**, 100208.

48 O. G. Salnikov, C. D. Assaf, A. P. Yi, S. B. Duckett, E. Y. Chekmenev, J.-B. Hövener, I. V. Koptyug and A. N. Pravdivtsev, *Anal. Chem.*, 2024, **96**, 11790–11799.

49 S. Knecht, A. N. Pravdivtsev, J. B. Hövener, A. V. Yurkovskaya and K. L. Ivanov, *RSC Adv.*, 2016, **6**, 24470–24477.

50 A. N. Pravdivtsev and J. B. Hövener, *Chemistry*, 2019, **25**, 7659–7668.

51 B. J. Tickner, J. S. Lewis, R. O. John, A. C. Whitwood and S. B. Duckett, *Dalton Trans.*, 2019, **48**, 15198–15206.

52 E. Caldeweyher, S. Ehlert, A. Hansen, H. Neugebauer, S. Spicher, C. Bannwarth and S. Grimme, *J. Chem. Phys.*, 2019, **150**, 154122.

53 B. Helmich-Paris, B. De Souza, F. Neese and R. Izsák, *J. Chem. Phys.*, 2021, **155**, 104109.

54 F. Neese, *J. Comput. Chem.*, 2003, **24**, 1740–1747.

55 G. L. Stoychev, A. A. Auer and F. Neese, *J. Chem. Theory Comput.*, 2017, **13**, 554–562.

56 M. Garcia-Ratés and F. Neese, *J. Comput. Chem.*, 2020, **41**, 922–939.

57 D. Bykov, T. Petrenko, R. Izsák, S. Kossmann, U. Becker, E. Valeev and F. Neese, *Mol. Phys.*, 2015, **113**, 1961–1977.

58 M. Garcia-Ratés and F. Neese, *J. Comput. Chem.*, 2019, **40**, 1816–1828.

59 F. Neese, F. Wennmohs, A. Hansen and U. Becker, *Chem. Phys.*, 2009, **356**, 98–109.

60 E. Caldeweyher, J.-M. Mewes, S. Ehlert and S. Grimme, *Phys. Chem. Chem. Phys.*, 2020, **22**, 8499–8512.

61 L. Wittmann, I. Gordiy, M. Friede, B. Helmich-Paris, S. Grimme, A. Hansen and M. Bursch, *Phys. Chem. Chem. Phys.*, 2024, **26**, 21379–21394.

62 E. Caldeweyher, C. Bannwarth and S. Grimme, *J. Chem. Phys.*, 2017, **147**, 034112.

63 S. Grimme, C. Bannwarth, S. Dohm, A. Hansen, J. Pisarek, P. Pracht, J. Seibert and F. Neese, *Angew. Chem., Int. Ed.*, 2017, **56**, 14763–14769.

64 G. L. Stoychev, A. A. Auer, R. Izsák and F. Neese, *J. Chem. Theory Comput.*, 2018, **14**, 619–637.

65 F. Neese, *Wiley Interdisc. Rev.: Comput. Mol. Sci.*, 2022, **12**, e1606.

66 F. Neese, *J. Comput. Chem.*, 2023, **44**, 381–396.

67 B. B. Mascitti, G. Zanoni, F. De Biasi, F. Rastrelli and G. Saielli, *Phys. Chem. Chem. Phys.*, 2025, **27**, 16326–16335.

68 *Mathematica, Version 14.0*, Wolfram Research, Inc., Champaign, IL, 2023.

69 C. D. Assaf, X. Gui, A. A. Auer, S. B. Duckett, J.-B. Hövener and A. N. Pravdivtsev, *J. Phys. Chem. Lett.*, 2024, **15**, 1195–1203.

70 I. Adelabu, J. Ettedgui, S. M. Joshi, S. Nantogma, M. R. H. Chowdhury, S. McBride, T. Theis, V. R. Sabbasani, M. Chandrasekhar, D. Sail, K. Yamamoto, R. E. Swenson, M. C. Krishna, B. M. Goodson and E. Y. Chekmenev, *Anal. Chem.*, 2022, **94**, 13422–13431.

71 R. W. Adams, S. B. Duckett, R. A. Green, D. C. Williamson and G. G. R. Green, *J. Chem. Phys.*, 2009, **131**, 194505.

72 K. L. Ivanov, A. N. Pravdivtsev, A. V. Yurkovskaya, H.-M. Vieth and R. Kaptein, *Prog. Nucl. Magn. Reson. Spectrosc.*, 2014, **81**, 1–36.

73 D. A. Barskiy, A. N. Pravdivtsev, K. L. Ivanov, K. V. Kovtunov and I. V. Koptyug, *Phys. Chem. Chem. Phys.*, 2016, **18**, 89–93.

74 S. Knecht, A. N. Pravdivtsev, J. B. Hövener, A. V. Yurkovskaya and K. L. Ivanov, *RSC Adv.*, 2016, **6**, 24470–24477.

75 W. Iali, S. S. Roy, B. J. Tickner, F. Ahwal, A. J. Kennerley and S. B. Duckett, *Angew. Chem., Int. Ed.*, 2019, **58**, 10271–10275.

76 A. S. Kiryutin, A. V. Yurkovskaya, H. Zimmermann, H. M. Vieth and K. L. Ivanov, *Magn. Reson. Chem.*, 2018, **56**, 651–662.

77 CCDC 2445882: Experimental Crystal Structure Determination, 2025, DOI: **10.5517/ccdc.csd.cc2n34fc**.

22936 | *Phys. Chem. Chem. Phys.*, 2025, **27**, 22924–22936

This journal is © the Owner Societies 2025